Dalton Transactions

ROYAL SOCIETY OF CHEMISTRY

PAPER

View Article Online
View Journal | View Issue

Cite this: *Dalton Trans.*, 2024, **53**, 10303

A combined theoretical and experimental approach to determine the right choice of co-ligand to impart spin crossover in Fe(II) complexes based on 1,3,4-oxadiazole ligands†

Sriram Sundaresan, [a] Julian Eppelsheimer,[a] Esha Gera,[b] Lukas Wiener,[a] Luca M. Carrella, [a] Kuduva R. Vignesh *[b] and Eva Rentschler *[a]

We present the synthesis of two new novel tetradentate ligands based on 1,3,4-oxadiazole, 2-(2-pyridyl)-5-[*N*,*N*-bis(2-pyridylmethyl)aminomethyl]-1,3,4-oxadiazole ($L^{TetraPy-ODA}$) and 2-(2-phenyl)-5-[*N*,*N*-bis(2-pyridylmethyl)aminomethyl]-1,3,4-oxadiazole ($L^{TetraPh-ODA}$). The ligands were used to prepare six mononuclear complexes [Fe^{II}($L^{TetraPy-ODA}$)(NCE)] (**C1–C3**) and [Fe^{II}($L^{TetraPh-ODA}$)(NCE)] (**C4–C6**) where E = S, Se or BH_3. In addition, the ligand $L^{TetraPy-ODA}$ was employed in the synthesis of a new di-nuclear complex [Fe^{II}_2($L^{TetraPh}$)]$(ClO_4)_4$·1 CH_3NO_2·1.5 H_2O (**C7**). Characterization of all complexes was carried out using single-crystal X-ray crystallography, elemental analysis, and infrared spectroscopy. Magnetic susceptibility measurements, performed in the temperature range of 2–300 K using a SQUID magnetometer, revealed spin crossover behaviour exclusively in the mononuclear complexes **C3** and **C6**, in which two monodentate $NCBH_3^-$ co-ligands coordinate. The presence of the lattice solvent was found to be crucial to the spin transition property, with complex **C3** exhibiting a switching temperature ($T_{1/2}$) of approximately 165 K and **C6** approximately 194 K. The other four mononuclear complexes **C1**, **C2**, **C4**, **C5**, as well as the dinuclear complex **C7** are locked in the high spin state over the measured temperature range. Density Functional Theory (DFT) calculations were performed on complexes **C1–C6** to rationalise the observed magnetic behaviour, demonstrating the significant effect of the NCS^-, $NCSe^-$ and $NCBH_3^-$ co-ligands ligands on the spin-crossover behaviour of the [Fe^{II}(L)(NCE)] complexes.

Received 17th April 2024,
Accepted 30th May 2024

DOI: 10.1039/d4dt01141d

rsc.li/dalton

Introduction

Iron chemistry is captivating in many ways from its abundance on Earth in the form of iron oxides, to its significant role in biology, where iron ions are essential for oxygen or electron transport processes in metalloproteins.[1,2] As scientists continue to explore its properties and applications, iron promises to remain a vital element in shaping our world. Its ready accessibility in the oxidation states +2 and +3, coupled with its ability to access higher oxidation states such as +6 and +7 through appropriate ligand selection, makes the iron ion an interesting candidate for diverse applications including catalysis and magnetism.[3,4]

One particularly fascinating phenomenon exhibited by iron ions in oxidation states +2 and +3 is spin-crossover (SCO), where electrons undergo an internal rearrangement of the orbital occupation in response to the external stimuli, allowing the metal ion to switch between two states.[5–8] This phenomenon, initially observed by Cambi and co-workers in Fe(III), has been more widely studied for Fe(II), due to the change in the electronic arrangement between a diamagnetic low spin state LS (S = 0) and a paramagnetic high spin state HS (S = 2).[5,9,10] Spin crossover is also observed for other *3d* metals such as Co(II), Mn(III) and Cr(II).[11–14] This bi-stability makes these candidates promising for various applications such as sensors, memory and displays.[15–19]

Fe(II) complexes based on 1,3,4-oxadiazoles are rarely reported in the literature for spin crossover. Some of us reported the first dinuclear Fe(II) complex based on 1,3,4-oxadiazole and successfully investigated the effect of the counter-ion ions.[20] In contrast, all attempts to further vary the ligand field strength by choosing different heterocyclic sidearms remained unsuccessful in observing the spin crossover behaviour. In all cases, the complex remained in the HS state

[a]*Department Chemie, Johannes-Gutenberg-Universität Mainz, Duesbergweg 10–14, 55128 Mainz, Germany. E-mail: rentschl@uni-mainz.de*
[b]*Department of Chemical Scienaces, Indian Institute of Science Education Research (IISER) Mohali, Sector-81, Knowledge City, S.A.S. Nagar, Mohali 140306, Punjab, India. E-mail: vigneshkuduvar@iisermohali.ac.in*

†Electronic supplementary information (ESI) available. CCDC 2348659–2348666. For ESI and crystallographic data in CIF or other electronic format see DOI: https://doi.org/10.1039/d4dt01141d

irrespective of the counterions chosen.[21] Klingele, Letard and co-workers in 2013 reported a mononuclear Fe(II) complex based on a bis-bidentate oxadiazole ligand and two NCS^- co-ligands. However, the complex remained in the HS state over the measured temperature window.[22] Later, in 2022, Herchel and co-workers further modified the bis-bidentate ligand to tune the ligand field strength and reported another mononuclear complex with two NCS^- co-ligands. Unfortunately, this complex also remained in the HS state over the measured temperature window.[23] Finally, some of us could recently report the first mononuclear Fe(II) spin crossover complex based on a tetradentate 1,3,4 oxadiazole ligand with two monodentate $NCBH_3^-$ co-ligands $[Fe(\mathbf{L}^{\mathbf{Tetra-ODA}})(NCBH_3)_2]\cdot 1.5\ CH_3OH$, where $\mathbf{L}^{\mathbf{Tetra-ODA}}$ is the tetradentate 2-(naphthalen-2-yl)-5-[*N*,*N*-bis(2-pyridylmethyl) aminomethyl]-1,3,4-oxadiazole ligand.[24] Given the extended pi system of the naphthalic substituent, which is known to be an antenna component in photoactive systems, the luminescence property of the complex, along with the synergistic effects of luminescence and spin crossover behaviour was investigated for this compound.[24] In the present manuscript, the tetradentate binding pocket of the previously reported ligand is kept constant, but the naphthalene moiety of the previously reported analogue is changed to pyridine and phenyl to investigate in more detail the effect of it on the SCO behaviour. The incorporation of pyridine in the ligand backbone also facilitated the synthesis of a new dinuclear Fe(II) complex based on 1,3,4-oxadiazole. Finally, the effect of other NCE (E = S and Se) co-ligand in tuning the spin crossover behaviour is also explored in the current study.

Results and discussion

Ligand synthesis

The two ligands 2-(2-pyridyl)-5-[*N*,*N*-bis(2-pyridylmethyl)aminomethyl]-1,3,4-oxadiazole ($\mathbf{L}^{\mathbf{TetraPy-ODA}}$) and 2-phenyl-5-[*N*,*N*-bis(2-pyridylmethyl)aminomethyl]-1,3,4-oxadiazole ($\mathbf{L}^{\mathbf{TetraPh-ODA}}$) were synthesised in high yields according to the ligand synthesis of $\mathbf{L}^{\mathbf{Tetra-ODA}}$, reported previously by some of us.[24] The main modification to the procedure was the use of appropriate pyridine-2-carboxylic acid hydrazide in the case of $\mathbf{L}^{\mathbf{TetraPy-ODA}}$ and phenyl-2-carboxylic acid hydrazide in the case of $\mathbf{L}^{\mathbf{TetraPh-ODA}}$ (Scheme 1). Both ligands were obtained in high yields 67% and 78%. The ligands obtained in both cases are fully characterized by ^{1}H NMR, ^{13}C NMR, COSY, HSQC and HMBC, infrared spectroscopy (Fig. S1–S12†).

Complex synthesis

All six mononuclear complexes **C1–C6** were prepared in a glovebox due to the air sensitivity of the precursor complexes used in this synthesis. Complexes **C1–C6** were prepared by dissolving equimolar ratios of the ligand with the corresponding NCE precursor complex in acetonitrile (**C1–C6**). Complex **C7** is prepared under aerobic conditions by dissolving one equivalent of the ligand with two equivalents of $Fe(ClO_4)_2$ salt in nitromethane. The complexes in all seven cases are obtained as crystals suitable for X-ray diffraction. The X-ray data for all seven complexes were collected from single crystals carefully picked from the mother liquor, whereas magnetic data were collected from the pure bulk powder, which was filtered and dried in air unless otherwise indicated. In all the cases, the complexes obtained are air-stable and have been characterized using a range of techniques including X-ray crystallography, elemental analysis, and infrared spectroscopy (Fig. S13–18†). Detailed information on the synthesis of each complex is given in the experimental section.

Structural description

Mononuclear complexes C1–C6. In all six cases, the coordination sphere is satisfied by a tetradentate 1,3,4-oxadiazole-based ligand with two NCE co-ligands where E = S, Se and BH_3.

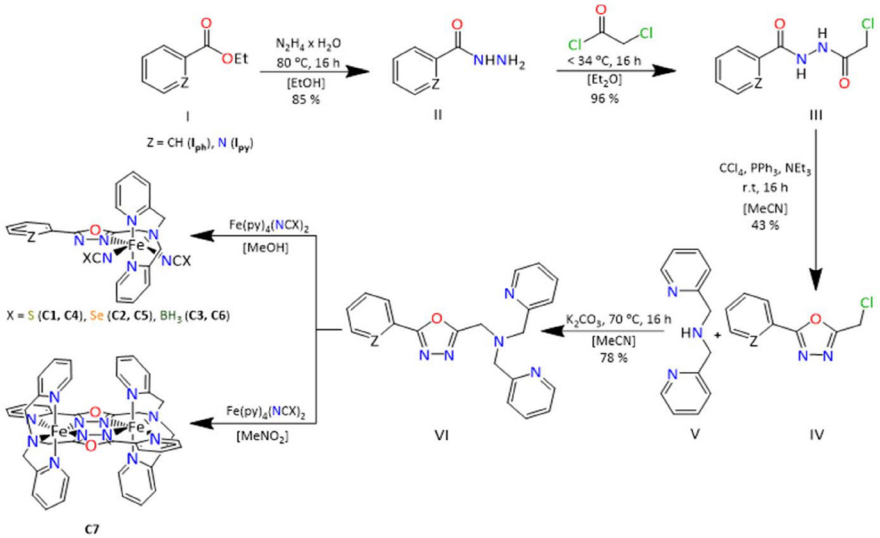

Scheme 1 Synthetic scheme of tetradentate ligand $\mathbf{L}^{\mathbf{TetraPy/Ph-ODA}}$ and complexes **C1–C7**.

In all the cases the two monodentate co-ligands are coordinated in the *cis* fashion similar to the $[Fe(\mathbf{L}^{\mathbf{Tetra-ODA}})(NCBH_3)_2]\cdot 1.5\ CH_3OH$ complex reported by some of us earlier.[24]

Complexes **C1** and **C2** both crystallise as yellow block-shaped single crystals from acetonitrile by slow evaporation. Crystallographic data was recorded at 120 K in both cases revealing that the complexes crystalise in the space group $P2_1/c$ in a monoclinic crystal system with four formula units in the unit cell. Crystallographic data are given in Table S1.† The asymmetric unit comprises a complex molecule with one molecule of acetonitrile in the case of **C1** (Fig. 1) and three acetonitrile in the case of **C2** (Fig. 1). The average metal-to-ligand bond distance in both cases is around 2.18 Å which is in the typical range for HS Iron(II) from the literature.[8,20,25,26] The octahedral distortion calculated for both complexes **C1** and **C2** are $\Sigma_O(FeN_6) = 102.3°$ and $\Sigma_O(FeN_6) = 100.3°$, respectively. Both complexes exhibit π–π stacking between the aromatic rings of the 2-picolylamine sidearms of adjacent molecules. The interplanar distance ranges from 3.94 Å to 4.03 Å and the interplanar angle ranges from $\theta = 15.8°$ to 23.9° (Fig. S22–S24† for **C1** and S27–32† for **C2**). The packing diagram of both **C1** and **C2** shows that due to the π-π stacking interaction between the aromatic rings, in both cases the complexes are packed in a 1-D chain-like structure along the *b*-axis. In the case of complex **C2**, a second π–π interaction is also observed between the pyridine bound to the oxadiazole and the 2-picolyl bound to the amine nitrogen of the neighbouring complex molecule by a T-shaped intramolecular interaction (Fig. S32†). This, in combination with the other π–π interaction (1-D chain formation), forms a cross-linked 2-D network in the case of **C2** (Fig. S27†).

Complex **C3** crystallises from acetonitrile in the space group *C*2/*c* with eight formula units per unit cell. The asymmetric unit comprises one molecule of the complex and one acetonitrile as in the case of **C1** (Fig. 1). The molecule is completed *via* symmetry operations. The average central metal donor distances measured at 173 K are around 2.18 Å, indicating HS Fe (II).[8,20,25,26] The crystallography parameters are tabulated in Table S2.† A low temperature structure measurement for complex **C3** was not possible.

Complexes **C4** and **C5** formed from the $\mathbf{L}^{\mathbf{TetraPh-ODA}}$ ligand with NCS^- and $NCSe^-$ co-ligands crystallised from acetonitrile in the *C*2/*c* space group in the monoclinic crystal system with eight formula units in the unit cell. The crystallographic data for both complexes and metal–ligand bond distances are tabulated in Table S3.† The asymmetric unit comprises one complex molecule with two solvent molecules. The X-ray crystallography data for both complexes are collected at 173 K (Fig. 2). The average metal-to-ligand bond distance is around 2.15 Å indicating the iron(II) to be in the HS state. The complex distortion from the ideal octahedral environment is calculated by the octahedral distortion parameter which is calculated for both complex **C4** and **C5** as 105.1° and 101°, respectively. Two different modes of π–π interactions are observed for complexes **C4** and **C5**. Intramolecular interaction can be seen between two picoline rings of the two neighbouring molecules can be observed which in turn forms a 1-D chain along the *b*-axis similar to the case of the **C2** discussed earlier (Fig. S37†). In addition to this, as seen in **C2** and **C3**, the complexes show a 2-D network formed by π–π interactions.

Complex **C6** is isolated from acetonitrile in the form of block-shaped single crystals by slow evaporation. The X-ray crystallography data for the complex were collected at two different temperatures of 120 K and 240 K. The X-ray data revealed that the complex crystallised in the *C*2/*c* space group (Fig. 2). The crystallographic data, along with the bond length for both temperatures, are summarized in Table S4.† The average metal-to-ligand bond length at 120 K is around 1.97 Å *vs.* 2.18 Å at 220 K, as shown in Fig. 3. The changes in the bond length, as well as an increase in the cell volume by 7%, indicate the complex undergoes a spin transition. The π–π interaction is very similar to the analogous compounds **C4** and **C5**, where a 1-D chain-like structure is formed along the *c*-axis, as well as the T-shape π–π interaction between two molecules can be found. It is worth noting that with the decrease in the volume at the lower temperature (120 K) the intermolecular distance became shorter. For example, the iron-iron distances in the 1-D chain along the *c*-axis are reduced from 13.191 Å to 12.271 Å by a change in the temperature (Fig. S48 and 49†).

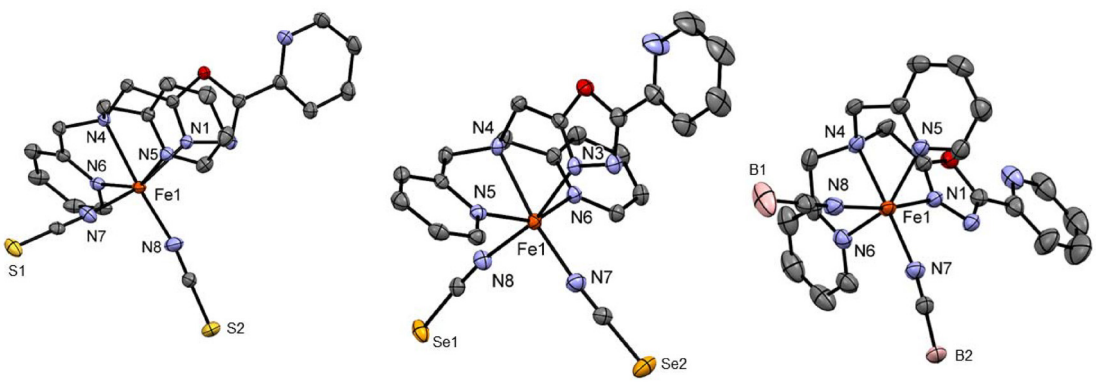

Fig. 1 Crystal structure of the complex $[Fe^{II}_2(\mathbf{L}^{\mathbf{TetraPy-ODA}})(NCS)_2]\cdot H_2O$, **C1** (left) and $[Fe^{II}_2(\mathbf{L}^{\mathbf{TetraPy-ODA}})(NCSe)_2]\cdot 0.15\ CH_3CN\cdot 1.5\ H_2O$, **C2** (middle) at 120 K and $[Fe^{II}_2(\mathbf{L}^{\mathbf{TetraPy-ODA}})(NCBH_3)_2]\cdot 2H_2O$, **C3** measured at 173 K . Hydrogen atom and solvent molecules are omitted for clarity.

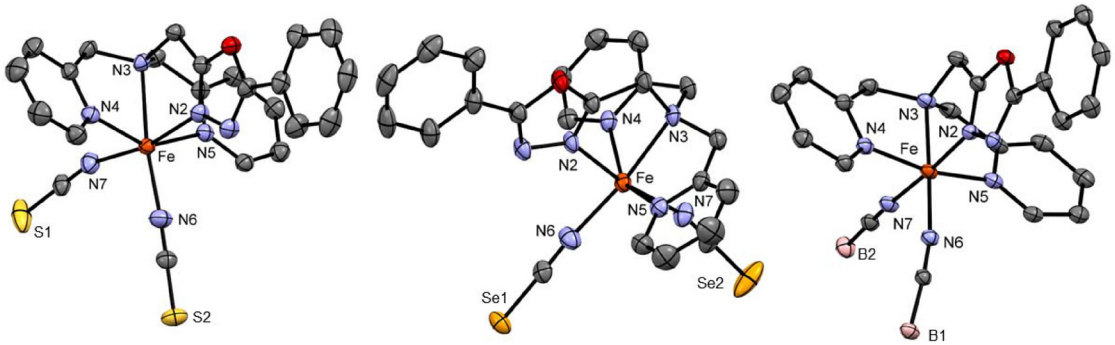

Fig. 2 Crystal structure of the complex $[Fe^{II}_2(L^{TetraPh-ODA})(NCS)_2]\cdot 1.75\ H_2O$, **C5** (left) and $[Fe^{II}_2(L^{TetraPh-ODA})(NCSe)_2]\cdot 0.4Et_2O\cdot H_2O$, **C6** (middle) at 173 K and $[Fe^{II}_2(L^{TetraPh-ODA})(NCBH_3)_2]\cdot 1.5\ H_2O$, **C7** measured at 120 K . Hydrogen atom and solvent molecules are omitted for clarity.

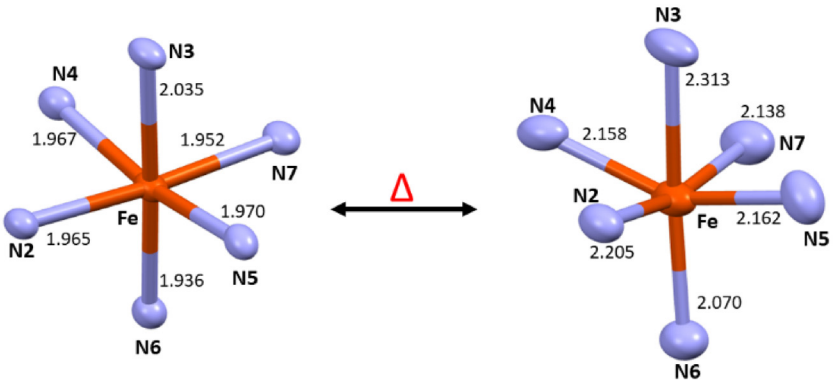

Fig. 3 Metal donor distances at 120–220 K for $[Fe^{II}_2(L^{TetraPh-ODA})(NCBH_3)]\cdot 1.5\ H_2O$.

Di-nuclear complex $[Fe^{II}_2(L^{TetraPy})](ClO_4)_4\cdot 1\ CH_3NO_2\cdot 1.5\ H_2O$ (C7). The ability of the ligand L^{Py-ODA} to form dimer successfully similar to our dimers reported with 1,3,4-Oxadiazole ligand was also explored.[20,21] Complex 7 was obtained as orange block-shaped crystals from nitromethane. The X-ray data recorded at 150 K reveals that the complex crystallises in the space group $P2_1/n$ in the monoclinic crystal system. All crystal data parameters are listed in Table S5.† The asymmetric unit comprises one ligand molecule coordinated to one iron centre and two perchlorate counterions (Fig. 4). The remaining excess electron density in the lattice is modelled as one nitromethane molecule in the crystal lattice. Both perchlorate molecules are disordered. As the remaining complex molecule is generated by symmetry just the coordination sphere of Fe1 is discussed in detail. The average metal-to-ligand bond length in the case of complex **C7** is 2.20 Å, which is in agreement with the values for HS Fe(II).[20,21,25] The octahedral distortion value is calculated to be $\Sigma_O(FeN_6)$ = 153.7°. This is a very high deviation from the ideal octahedral coordination and can be explained by the N4–Fe1–N1 *cis*-angle (125.72(4) °) and the N5–Fe1–N6 *trans*-angle (143.83(5) °), which differ very much from 90° and 180°, respectively. This distortion is consequently reflected in all *cis*-angles to the apical pyridine rings, which results in the high value octahedral distortion which also leads to stabilize the complexes in HS state.

Similar distortions were observed in the earlier reported dimeric thiadiazole and oxadiazole-based iron(II) complexes.[20,21,27,28]

Solid state magnetic data. The temperature-dependent magnetic susceptibility behaviour for all seven complexes (**C1–C7**) was determined with pure microcrystalline samples in all cases from 2–400 K, in both heating and cooling modes.

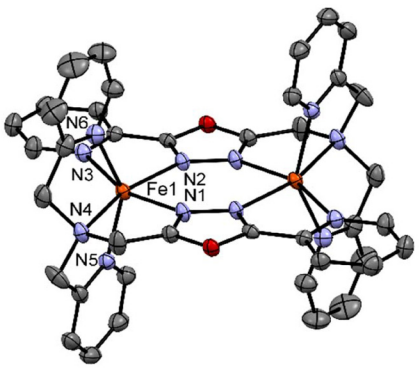

Fig. 4 Crystal structure of the complex $[Fe^{II}_2(L^{TetraPy})](ClO_4)_4\cdot CH_3NO_2\cdot 1.5\ H_2O$ at 150 K. Hydrogen atom and counter ions and solvent molecules are omitted for clarity.

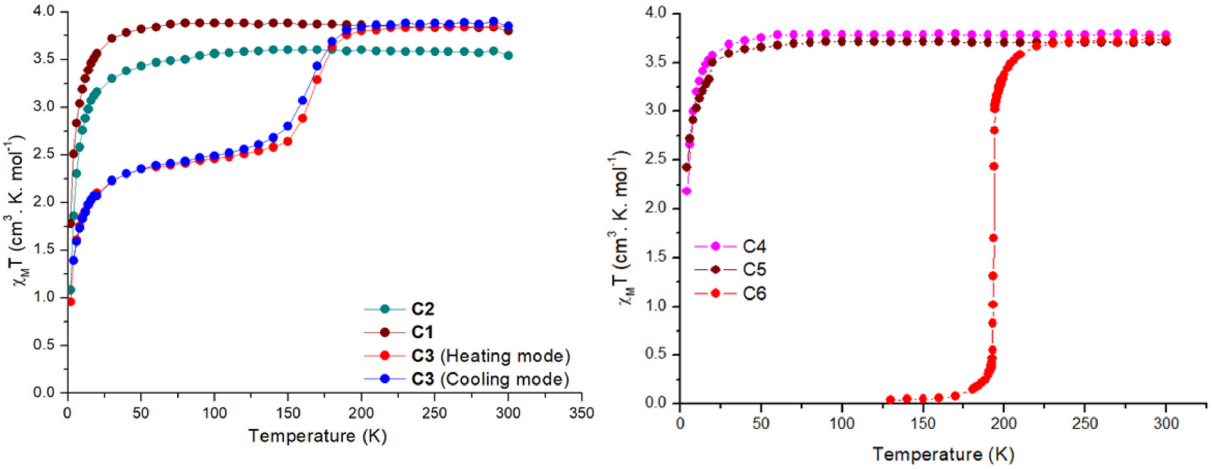

Fig. 5 $\chi_M T$ *vs. T* for complexes **C1–C3** (left) **C4–C6** (right). The dots are the data points, and the line is just a guide for the eye.

Complexes **C1**, **C2**, **C4**, and **C5** show a high spin state down to low temperatures with $\chi_M T$ values of 3.5–3.8 $cm^3\ mol^{-1}\ K$, as shown in Fig. 5. The determined magnetic moments are in agreement with the literature values for high spin mononuclear Fe(II) complex ranging from 3–4 $cm^3\ mol^{-1}\ K$.[6,7,29] This finding nicely agrees with the analysis of the bond lengths determined from the X-ray data for Fe(II) HS in all cases showing an average bond length of 2.18 Å. When the temperature is lowered, the $\chi_M T$ values remain almost constant down to 50 K. The drop below 50 K is attributed to the combination of weak intermolecular dipolar interaction and weak zero-field splitting of the Fe(II) centre in all the above cases.

In contrast, complexes **C3** and **C6** show a temperature-dependent spin crossover behaviour as can be seen in Fig. 5. Complex **C3** shows an abrupt change in magnetic moment, expressed in $\chi_M T$, around 165 K, while complex **C6** abruptly changes its magnetic behaviour just below 200 K. When the magnetic data was collected in the cooling mode from 300–2 K in the polycrystalline air-dried sample, the $\chi_M T$ value remained constant at 3.85 $cm^3\ mol^{-1}\ K$ until 200 K. Thereafter a drop in the $\chi_M T$ value to 2.68 $cm^3\ mol^{-1}\ K$ at 140 K is seen. This behaviour can be attributed to an incomplete SCO where approximately only 50% of the sample is switched to the LS state. Further cooling below 40 K leads to a further sharp drop in the $\chi_M T$ value to 0.95 $cm^3\ mol^{-1}\ K$ at 2 K, attributed to the combination of weak intermolecular dipolar interaction and zero-field splitting of the HS iron centre. Structural elucidation at low temperature of 100 K would have been very beneficial but unfortunately this was not possible. For the cooling mode the $T_{1/2}$ is estimated to be 160 K. When the magnetic data was collected in the heating mode from 2–300 K the $\chi_M T$-curve profile remained the same with a slight shift in the $T_{1/2(up)}$ to 170 K. This change in $T_{1/2}$ shows a small thermal hysteresis of approximately 5 K centred around 165 K, as seen in Fig. 5.

The effect of the lattice solvent in tuning the spin transition temperature in the solid state is well investigated in the SCO literature.[25,28,30] In many cases the spin transition is dependent on the presence of the lattice solvent, and when removed, the complex is locked in one spin state or the $T_{1/2}$ of the complexes is shifted. In the case of the complex **C3** the lattice solvent of the bulk is water. Since complex **C3** exhibited an incomplete spin transition with a small hysteresis, the effect of the lattice solvent in tuning the spin transition temperature was investigated using a freshly prepared microcrystalline sample from the mother liquor (acetonitrile) with no exposure to air (Fig. S57†). The $\chi_M T$ data was first recorded in the cooling mode from 300–70 K, followed by 70–400 K, and then from 400–2 K. In the first cooling cycle, the $\chi_M T$ value stayed constant at 3.8 $cm^3\ mol^{-1}\ K$ from 300–200 K with a sudden sharp decrease to 0.24 $cm^3\ mol^{-1}\ K$ at 150 K. In the subsequent warming mode, the magnetic behaviour was unaltered until 400 K with a $T_{1/2}$ of 165 K (Fig. S57†). However, when the lattice solvent acetonitrile was evaporated at 400 K and the sample was cooled to 2 K, the SCO behaviour of the complex was lost and complex **C3** was locked in HS state over the measured temperature range until 30 K. A small rise in the $\chi_M T$ around 30 K is due to the crystal orientation effects at low temperature.

Complex **C6** shows the spin transition, as indicated by bond length changes observed by variable temperature X-ray measurements. A $T_{1/2}$ temperature of 194 K is estimated from the abrupt change in the magnetic moment upon lowering the temperature (Fig. 5). The lattice solvent of the bulk sample was water. To obtain the effects of the lattice solvent, a freshly prepared sample from the mother liquor with no exposure to air was used for the magnetic measurements. The $\chi_M T$ data were recorded in the temperature sequence 300–130–400–2 K. When measured in the cooling mode the $\chi_M T$ value at 300 K was 3.72 $cm^3\ mol^{-1}\ K$ and remained constant down to 250 K. Below 250 K, a very abrupt drop in the magnetic moment to a value of 0.04 $cm^3\ mol^{-1}\ K$ at 130 K was observed. The magnetic profile was the same when the data was recorded in the warming mode. However, after the lattice solvent acetonitrile

was removed at 400 K, the complex was locked in HS over the measured temperature window (Fig. S56†).

Finally, the magnetic data collected for the complex **C7** from 300–2 K revealed that the complex stays in the HS state over the entire measured temperature window (Fig. S58†). This was also shown by the temperature independent metal ligand bond distances for both iron centres as observed by X-ray crystallography. The $\chi_M T$ value for complex **C7** at 300 K is 7.43 cm^3 mol^{-1} K slightly decreasing to 7.26 cm^3 mol^{-1} K at 40 K. Below 40 K a drop in the magnetic moment to 4.14 cm^3 mol^{-1} K can be attributed to a combination the combination of weak intermolecular dipolar interaction and zero-field splitting as well as possible weak anti-ferro magnetic coupling effects between the iron centres.

By changing the naphthalene side group in the previously reported complex with the naphthalene ligand [Fe($\mathbf{L}^{\mathbf{Tetra-ODA}}$)$(NCBH_3)_2$]·1.5 CH_3OH to pyridine or phenyl groups, the $T_{1/2}$ value of complexes C3 and C6 changed as expected. In the case of **C3** with the pyridine ligand backbone, the $T_{1/2}$ is around 165 K which is a change in $T_{1/2}$ of about 42 K to lower temperatures. In the phenyl complex **C6**, which is a closer analogue to the previously reported naphthalene complex, the shift of $T_{1/2}$ is only 13 K towards lower temperatures. The shift in the $T_{1/2}$ indicates the tuning of the ligand field strength by choice of different aromatic rings.

In addition to the changes made to the ligand backbone, the co-ligands were varied. Besides the $NCBH_3^-$ ligand the monodentate co-ligands $NCSe^-$ and NCS^- were used to fine-tune the spin transition temperature. All NCE co-ligands are frequently studied in spin crossover research to tune the ligand field strength.[25,26,31,32] Of these three monodentate co-ligands, NCS^- has the strongest coordination ability with an index a^{TM} of 1.6, as shown by Alvarez's careful data mining of the CCDC database. In comparison, $NCSe^-$ has 1.4 and $NCBH_3^-$ has 1.0.[33] The ligand field strength decreases with the increase in the coordination ability as nicely shown in the recent work by Cirera and Paesani.[34] Unfortunately, in the present study, all complexes except **C3** and **C6** were invariant in the HS state over the measured temperature range regardless of the change in NCE ligands. The complex **C3** and **C6** showed solvent-dependent SCO behaviour as discussed earlier. The two other mononuclear complexes reported in the literature with 1,3,4-oxadiazole-based ligands stay in the HS state. In both cases the co-ligand was NCS^-.[22,23]

From the current work and the previously reported [Fe($\mathbf{L}^{\mathbf{Tetra-ODA}}$)$(NCBH_3)_2$]·1.5 CH_3OH complex, it is clear that the 1,3,4-oxadiazole based ligand in combination with the $NCBH_3^-$ co-ligand creates appropriate ligand field for the spin transition to occur.

It should be noted that comparisons with the previously reported naphthalene complex [Fe($\mathbf{L}^{\mathbf{Tetra-ODA}}$)$(NCBH_3)_2$]·1.5 CH_3OH and other literature complexes should be made with caution as it is well-known from the literature that the crystal packing effects play a key role in determining the spin transition temperature in the solid state.[25,28,30] The role of the lattice solvent in spin crossover materials influences various aspects of the SCO behaviour including cooperative effects.[24,25,28,30] Interactions between the solvent and the spin crossover complexes may facilitate or hinder the structural rearrangements required for spin state switching. Understanding and controlling these interactions are essential for the design and optimization of spin crossover materials. The previously reported [Fe($\mathbf{L}^{\mathbf{Tetra-ODA}}$)$(NCBH_3)_2$]·1.5 CH_3OH complex had methanol as the lattice solvent whereas the newly prepared analogues complexes **C3** and **C6** have acetonitrile as the lattice solvent. The crucial role of the lattice solvent in imparting the SCO behaviour in the solid state is also thoroughly investigated, since in both cases **C3** and **C6** the complexes lose their spin transition ability and are locked in the HS state, but in the analogues [Fe($\mathbf{L}^{\mathbf{Tetra-ODA}}$)$(NCBH_3)_2$]·1.5 CH_3OH complex reported earlier there is only a slight shift in the $T_{1/2}$ from 207 to 210 K (the slight shift might also be due to residual solvent still present in the crystal lattice).[24] The effect of ligand substituents and co-ligands in tuning the SCO behaviour is further probed by DFT calculations.

Predicting the SCO behaviour of C1–C6 using exchange–correlation functionals. Density Functional Theory (DFT) calculations were performed to predict the ground state of **C1–C6** complexes and to understand their spin-crossover character. The crystallographic geometries of all six iron(II) complexes were optimized followed by frequency calculations to predict the DFT computed thermodynamic parameters and the transition temperature ($T_{1/2}$) values. The performed DFT calculations are limited to gaseous phase species and do not account for crystalline, solvent, or packing effects; nonetheless, the computed values yield the exact spin ground states as well as support the electronic structure of the complexes. The optimization calculations using DFT methods are highly functional dependent according to the percentage of Hartree–Fock exchange. Thus, we performed calculations using two different hybrid functionals, such as B3LYP and B3LYP* where the exact exchange is 20% and 15% respectively. The choice of these two particular functionals is based on the following reasons: (a) B3LYP provides structures that exhibit good agreement with X-ray structure findings, making it the preferred functional for spectroscopic parameter computation; (b) B3LYP* hybrid functional is better for predicting both the exact ground state and the energy gap between the two spin states (ΔE_{HS-LS}).[35,36]

For the X-ray structures of complexes that were acquired at various temperatures, we did geometry optimization to understand the influence of spin-states on the geometrical parameters. It's important to clarify that optimised geometries are more symmetrical than X-ray structures. For instance, the optimised HS and LS structures are actually modelled at particular spin states, not the temperature-dependent ones. The DFT-optimised structures of **C1–C6** using both B3LYP and B3LYP* hybrid functionals are shown in Fig. 6, S59 and S60† with some of the selected bond parameters of the first coordination environment. Tables 1 and S6† summarise the X-ray structural parameters and the computed structural parameters for **C1–C6** using B3LYP* and B3LYP, respectively. The structural parameters of the optimized structures using both functionals are

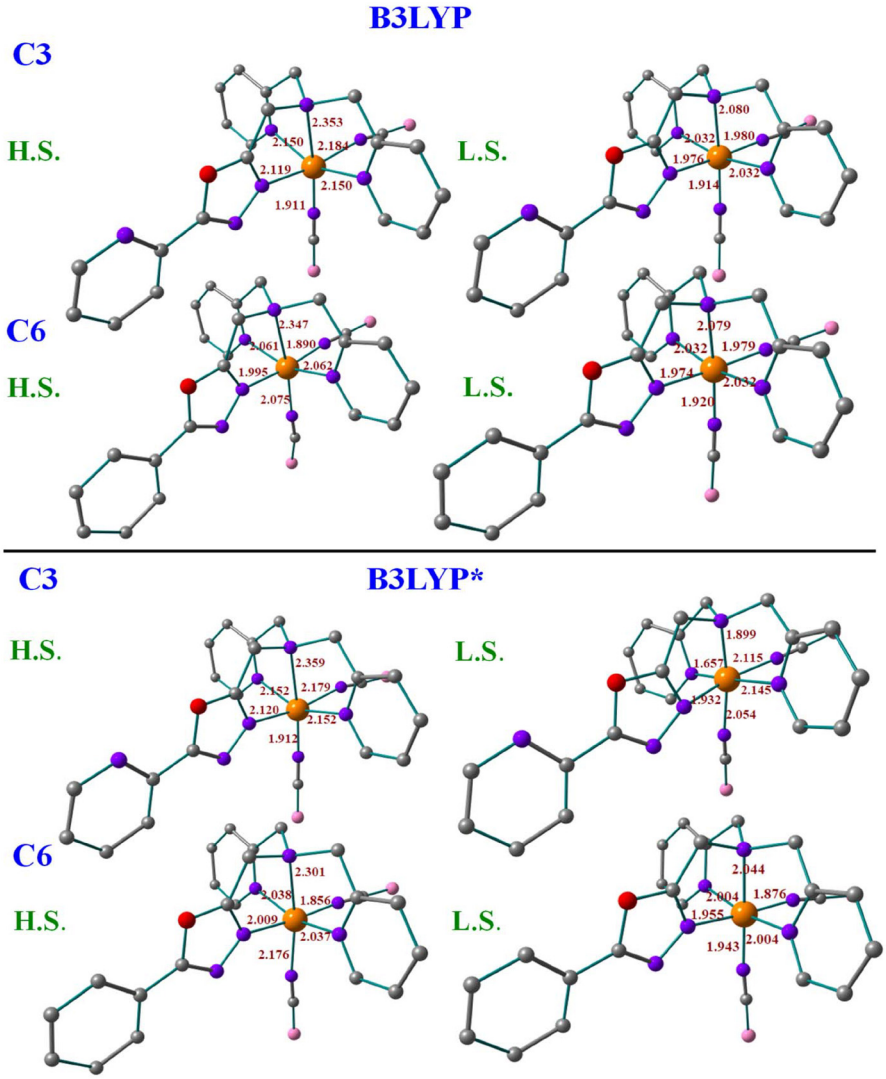

Fig. 6 Optimized structure with B3LYP & B3LYP* hybrid functional along with some selected bond parameters for complexes **C3** and **C6**. Colour code: Orange = Fe (Iron), Purple = N (Nitrogen), Red = O (Oxygen), Grey = C (Carbon), Pink = B (Boron), and hydrogen atoms are omitted for clarity.

Table 1 X-ray structural parameters with the B3LYP* computed parameters for complexes **C1**, **C2**, **C3**, **C4**, **C5** and **C6** (see Fig. 1 and 2 for atom numbering)

Structural parameter	**C1**			Structural parameter	**C2**			Structural parameter	**C3**		
	EXP	HS	LS		EXP	HS	LS		EXP	HS	LS
Fe–N1	2.227	2.129	1.966	Fe–N3	2.204	2.133	1.964	Fe–N1	2.217	2.120	1.932
Fe–N4	2.295	2.321	2.066	Fe–N4	2.311	2.369	2.065	Fe–N4	2.281	2.359	1.899
Fe–N5	2.220	2.161	2.011	Fe–N5	2.170	2.167	2.013	Fe–N5	2.163	2.152	1.657
Fe–N6	2.204	2.039	1.859	Fe–N6	2.176	2.166	2.013	Fe–N6	2.173	2.152	2.145
Fe–N7	2.101	2.161	2.011	Fe–N7	2.062	1.891	1.896	Fe–N7	2.071	1.912	2.054
Fe–N8	2.030	1.954	1.880	Fe–N8	2.105	2.195	1.881	Fe–N8	2.137	2.179	2.115
Angle N6–Fe–N8	97.94	96.08	97.80	Angle N7–Fe–N8	95.41	95.01	91.38	Angle N7–Fe–N8	92.97	93.08	92.45
Structural parameter	**C4**			Structural parameter	**C5**			Structural parameter	**C6**		
	EXP	HS	LS		EXP	HS	LS		EXP	HS	LS
Fe–N2	2.184	2.152	1.980	Fe–N2	2.171	1.962	1.961	Fe–N2	1.965	2.009	1.955
Fe–N3	2.303	2.373	2.076	Fe–N3	2.294	2.349	2.064	Fe–N3	2.035	2.301	2.044
Fe–N4	2.210	2.170	2.013	Fe–N4	2.207	2.139	2.013	Fe–N5	1.970	2.037	2.004
Fe–N5	2.217	2.171	2.016	Fe–N5	2.205	2.139	2.013	Fe–N6	1.936	2.176	1.943
Fe–N6	2.058	1.874	1.835	Fe–N6	2.065	1.917	1.896	Fe–N7	1.952	2.301	1.876
Fe–N7	2.095	2.109	1.845	Fe–N7	2.091	1.843	1.882	Fe–N8	1.967	2.038	2.004
Angle N7–Fe–N6	96.34	92.21	92.80	Angle N6–Fe–N7	95.03	93.73	91.33	Angle N6–Fe–N7	89.85	94.08	88.78

in good agreement with the X-ray structural parameters, especially the B3LYP computed parameters are much closer.[37] The computed structural parameters of the high-spin (HS; S = 2) state of **C1**, **C2**, **C4**, and **C5** are in close resemblance with the X-ray structural parameters, whereas the mix of both Low-spin (LS; S = 0) state and HS state parameters of **C3** and **C6** are matching with the X-ray structural parameters. This indicates that the complexes **C1**, **C2**, **C4**, and **C5** possess the HS ground state (Fig. S61†) and are unlikely to show SCO behaviour, and the **C3** and **C6** complexes are likely to show SCO behaviour if the energy gap between HS–LS is going to be in the expected range of SCO behaviour.[38] The computed bond parameters indicate how the distortion in the coordination sphere in the real structure is partly caused by solid-state processes.[38]

The DFT computed energies of the Fe(II) centre in the high-spin (S = 2) quintet state and the low-spin (S = 0) singlet state using B3LYP and B3LYP* functionals for all the complexes are shown in Fig. S61 and 7,† respectively. The B3LYP functional predicts HS as the ground state for **C1**, **C2**, **C4**, and **C5** and LS as the ground state for **C3** and **C6** complexes. The B3LYP computed energy gap between the HS–LS is found to be 82.9, 20.2, −242.1, 83.1, 85.7 and −280.9 kJ mol^{-1}, respectively, for complexes **C1**, **C2**, **C3**, **C4**, **C5** and **C6** (Fig. S61†). These energy gaps confirm that the NCS^- and $NCSe^-$ ligated complexes **C1**, **C2**, **C4**, and **C5** possess HS as the ground state and are unlikely to show spin-crossover, whereas the $NCBH_3^-$ ligated **C3** and **C6** are likely to show SCO behaviour since they possess LS as the ground state. This is in line with the experimental prediction of SCO behaviour for complexes **C3** and **C6**. However, the HS states of **C3** and **C6** are not in the thermally accessible region from the ground LS state (−242.1 and −280.9 kJ mol^{-1}) to facilitate the SCO phenomenon to occur, and this gap is expected to be in the −33 to 0 kJ mol^{-1} (−8 to 0 kcal mol^{-1}) range.[38] Though the B3LYP hybrid functional predicts the expected ground state for all these complexes, the energy gap between the HS–LS states is overestimated for the SCO complexes **C3** and **C6**. We assume that the amount of Hartree–Fock exchange (20%) in the B3LYP hybrid functional is large for predicting the correct energy gap between the HS–LS. The spin-state splitting is highly influenced by the percentage of HF exchange in hybrid functionals and it was evident from the previous study that the alteration in the %HF exchange in B3LYP helped them to comprehend the impact this had on the SCO properties of $[Fe(bik)_2(NCX)_2]$ (bik = bis(1-methylimidazol-2-yl)ketone); (X = S and Se) complexes.[36] It was mentioned that the reduction in the percentage of HF exchange in hybrid functional would help in attaining the exact ground state as well as the reasonable HS–LS energy gap; especially the B3LYP* (15%) is found to be an excellent one in predicting the SCO behaviour.[39–41]

Thus, we also optimised the geometry of all the complexes using B3LYP* functional which predicts HS as the ground spin state for NCS^- ligated complexes **C1** and **C4**, and LS as the ground state for $NCSe^-$ and $NCBH_3^-$ ligated complexes **C2**, **C3**, **C5** and **C6**. The B3LYP* functional predicts the following HS–LS energy gap: 9.8, −6.5, −15.2, 45.5, −28.2 and −43.8 kJ mol^{-1} for complexes **C1**, **C2**, **C3**, **C4**, **C5** and **C6**, respectively (Fig. 7). These energy gaps indicate that the NCS^- ligated complexes **C1** and **C4** do not show spin transition characteristics, whereas the $NCSe^-$ and $NCBH_3^-$ ligated **C2**, **C3**, **C5** and **C6** are likely to show SCO behaviour. This computational observation is in accordance with the experimental observation which predicts SCO behaviour for $NCBH_3^-$ ligated **C3** and **C6** complexes, whereas it is absent for NCS^- ligated **C1** and **C4** complexes. The B3LYP* computed energy difference of the HS–LS states for complexes **C2** and **C5** indicates that these complexes could also exhibit SCO behaviour, which contradicts the experimental observations suggesting no SCO behaviour. The discrepancy was attributed to the fact that the calculations were performed in the gas phase, exclusion of intermolecular interactions and lattice effects which are known to significantly influence the spin-state energetics.[42] Unlike B3LYP, the B3LYP* predicts the reasonable HS–LS energy gap for the $NCBH_3^-$ ligated **C3** and **C6** complexes which is in the ideal energy gap of −33 to 0 kJ mol^{-1} for **C3**, but it slightly falls outside the expected range for **C6** for the SCO behaviour to occur. Finally, the B3LYP* is found to be better compared to the B3LYP in predicting the ground state values as well as the SCO behaviour in the studied complexes. Thus, we further attempted to calculate the transition temperature ($T_{1/2}$) using only the B3LYP* functional for the SCO **C3** and **C6** complexes and compared them with the experimentally measured transition temperature ($T_{1/2}$). Still, this must be taken with caution as we are aware from the experimental data C3 and C6 for which B3LYP* predicts a LS ground state in the absence of lattice solvent in both cases, are also stabilised in the HS state. The predicted results B3LYP* must be validated with appropriate experimental data to know the role of intramolecular interactions, such as lattice solvent and packing effects. These play a very crucial role in SCO and cannot be accounted for in gas phase calculations.

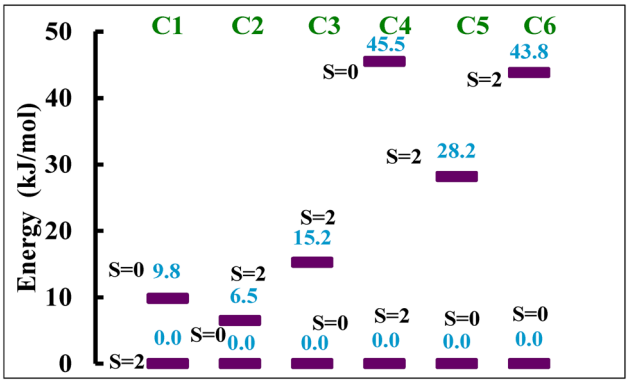

Fig. 7 Energy difference in kJ mol^{-1} between two spin states computed with B3LYP* for all six complexes.

To estimate the transition temperature ($T_{1/2}$), we calculated the thermodynamic parameters such as ΔH (H_{HS}–H_{LS}) and ΔS (S_{HS}–S_{LS}) based on the frequency calculations over the optimized coordinates and Table 2 summarises these values.

Table 2 B3LYP* calculated thermodynamic parameters with the transition temperature ($T_{1/2}$) in Kelvin for **C3** and **C6**

Thermodynamic parameters	C1	C2	C3	C4	C5	C6
ΔH (HS–LS) kJ mol^{-1}	−4.6	9.6	45.6	−6.2	−4.2	26.3
ΔS (HS–LS) J mol^{-1} K^{-1}	33.4	51.8	274.2	63.1	−43.5	160.1
$T_{1/2}$ (K) = $\Delta H/\Delta S$	—	—	166	—	—	164

These computed values align with the experimental findings for the reported Fe^{II} spin crossover compounds.[7,32,43] Vibronic entropy always favours the high-spin state; strong field ligands that energetically favour the low-spin state lose more to vibronic entropy. These estimated entropy and enthalpy values are highly dependent on the π-acceptor abilities, where these values are more pronounced for the complexes **C3** and **C6** which possess the moderate field $NCBH_3^-$ ligands and smaller for the complexes **C1** and **C4** which possess comparatively weaker field NCS^- ligand. This indicates that the π-acceptor abilities and the ligand field strength in comparison to the NCX (X = S/Se) ligand are comparatively better for the $NCBH_3^-$ ligated which imposes the SCO behaviour. Furthermore, the $T_{1/2}$ is estimated using these thermodynamic parameters and the formula $T_{1/2} = \Delta H/\Delta S$ for **C3** and **C6**.[35] The computed transition temperature ($T_{1/2}$) of 166K and 164 K for complexes **C3** and **C6**, respectively are in good agreement with the experimentally determined $T_{1/2}$ value of 165 K and 194 K. These results further support that the B3LYP* is a useful functional in determining the SCO behaviour.[38–41]

The π-acceptor abilities of these ligands are also reflected in the spin-density calculations. A spin-density value of *ca.* 4.038–4.168 has been found on the Fe(II) centres of **C1**, **C2**, **C3** and **C4** complexes in their high-spin structures which indicates the Fe(II) centres gain spins from the first coordinated atoms of the 1,3,4-oxadiazole ligand due to ligand-to-metal donor ability. Whereas a spin density value of *ca.* 2.60–2.82 has been found on the Fe(II) centres of **C5** and **C6** complexes which suggests that the metal-to-ligand spin delocalisation occurring to the first coordinated atoms of the 1,3,4-oxadiazole ligand and the NCE ligand. The net spin densities of the coordinated nitrogen atoms of NCS^-, $NCSe^-$, and $NCBH_3^-$ have spin densities of *ca.* −0.11 to 0.002 and −0.232 to 0.17 for complexes **C1** and **C4**, −0.196 to 0.160 and 0.135–0.194, for complexes **C2** and **C5**, 0.085–0.120 and −0.008 to 0.225 for complexes **C3** and **C6**, respectively. Similarly, the E donor atoms of NCE have spin densities of *ca.* −0.36 to −0.2 for the S atom, −0.78 to 0.6 for the Se atom, and −0.9 to 0.2 for the S atoms in their respective complexes. These small spin values of the first coordination sphere and the predominant spin values of the E donor atoms suggest a more pronounced π-acceptor ability for these $^-$NCE ligands towards the metal centre. The B3LYP* computed spin-density plots of **C3** and **C6** are shown in Fig. 8 and spin-density plots of the remaining complexes are shown in Fig. S62.† Moreover, these spin density values indicate that the two sets of complexes with three different $^-$NCE ligands can vary significantly in terms of structural and electronic alteration resulting in different SCO properties.[7,40]

The orbital splitting and the spin pairing energy can highly influence the spin ground state.[7,40] Thus, to get further insights into the possibility of spin-pairing energy in **C3** and **C6**, the *d*-based orbitals at their respective high-spin states have been computed and the eigenvalue plot with their energies is shown in Fig. 9. The B3LYP* calculated electronic configurations for the complexes **C3** and **C6** are as follows $(d_{xy})^2(d_{xz})^1(d_{yz})^1(d_{z^2})^1(d_{x^2-y^2})^1$ and $(d_{yz})^2(d_{xy})^1(d_{xz})^1(d_{z^2})^1(d_{x^2-y^2})^1$, respectively. The red arrow represents the spin-up (α) electrons whereas the green arrow represents the spin-down (β) electrons. For **C3**, the energy difference between the t_{2g}-like and e_g-like orbitals is around 168.74 kJ mol^{-1}, while it is approximately 33.28 kJ mol^{-1} for **C6**. The spins in the d_{xz} and d_{yz} orbitals must couple to generate the low-spin complex. The $NCBH_3$ coordination has a significant impact on both orbitals since these t_{2g}-like and e_g-like orbitals energy gap is extremely small which leads to the SCO behaviour in **C3** and **C6**. This results credence to the hypothesis that ligands with weak π-type interactions are the best choices for ligands for tuning the SCO characteristic.[37]

Stronger delocalization is facilitated by the C-atom of the phenyl ring near the oxalate ring ($\mathbf{L^{TetraPh-ODA}}$) which pos-

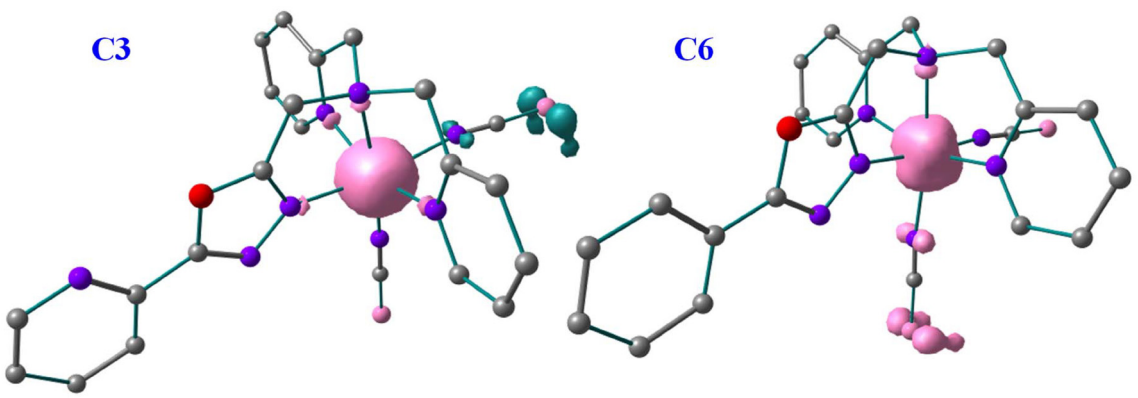

Fig. 8 Spin density diagram for complex **C3** and **C6** in High Spin state with B3LYP* optimised geometry.

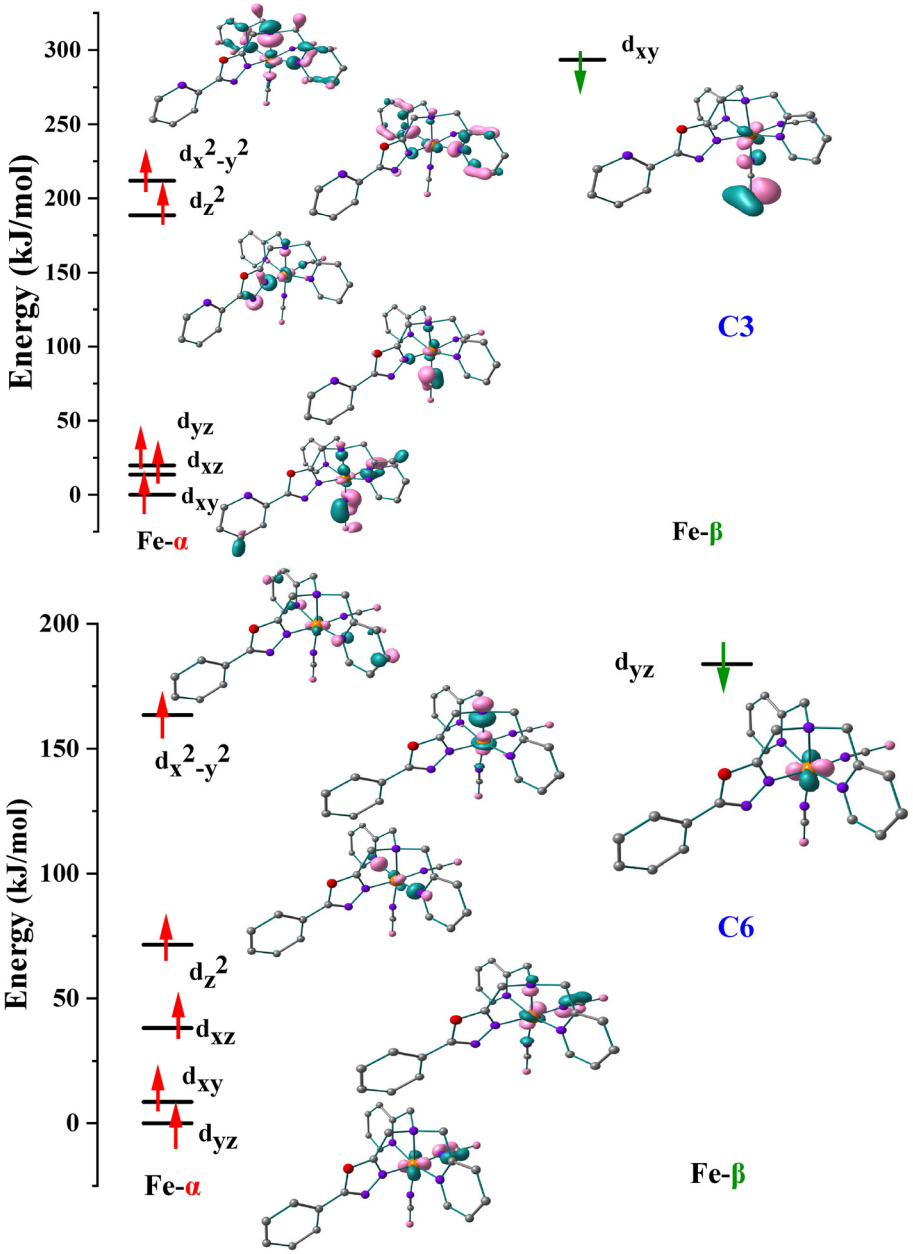

Fig. 9 Eigenvalue plot computed for **C3** and **C6**. Here, α and β represent spin-up and spin-down configurations. The energies are scaled to the lowest spin-up orbitals in each case.

sesses a spin value of 0.0033 in **C6**, whereas the N-atom of pyridine ($\mathbf{L}^{\mathbf{TetraPy-ODA}}$) possesses a spin value of 0.0016 in **C3**, which also specifically disturb the energies of the d_{xz} and d_{yz} orbitals. The d_{xz}/d_{yz} orbitals in the case of **C6** are considerably destabilized compared to **C3**, resulting in a narrower t_{2g}-e_g gap. Strong delocalization of $\mathbf{L}^{\mathbf{TetraPh-ODA}}$ to the Fe centre (Fig. 9) also enhances the pairing energy compared to the $\mathbf{L}^{\mathbf{TetraPy-ODA}}$ analogues, which compensates for the lower t_{2g}-e_g gap leads to the observation of SCO at a relatively higher temperature. This is because the SCO properties are correlated with both the crystal-field splitting and the pairing energy.

Conclusion

In conclusion, we have prepared two new tetradentate ligands $\mathbf{L}^{\mathbf{TetraPy-ODA}}$ and $\mathbf{L}^{\mathbf{TetraPh-ODA}}$ based on 1,3,4-Oxadiazole. We have also prepared six mononuclear complexes **C1–C6** with three different NCE co ligands where E = S (**C1**, **C4**), Se (**C2**, **C5**) and BH_3 (**C3**, **C6**). Complexes with $NCBH_3^-$ co-ligands with both the ligands (**C3** and **C6**) exhibit SCO behaviour. The SCO behaviour is dependent on the lattice solvent in both the cases which is thoroughly investigated. In comparison to the previously reported analogues complex with $NCBH_3^-$ co-ligand, the change from the naphthalene to phenyl did not affect the

ligand as much as expected and the $T_{1/2}$ remains close to each other but in the case of ligand $\mathbf{L}^{\mathbf{TetraPy-ODA}}$ the $T_{1/2}$ values indicate the ligand field is well reduced. This comparison has to be also taken with caution as the small changes in the crystal lattice and packing might affect the SCO behaviour. In addition to this, the di-nuclear complex **C7** prepared stays in the HS state over the measured temperature window. The existence of a spin transition in **C3** and **C6** is supported by DFT calculations performed on the electronic structures of both the low-spin and high-spin structures. To precisely replicate the HS–LS gap for all the complexes, two different functionals such as B3LYP and B3LYP* having different percentages of HF exchange were utilized for the calculations. The computed energy gap values using the B3LYP* functional, the one with a smaller percentage of HF exchange, yielded better results that are also in excellent agreement with the experimental observations. Furthermore, in the $NCBH_3^-$ ligated complexes, because of its poor π-donor abilities which in turn results in a greater ligand field, and these effects support a higher spin-transition temperature in the $NCBH_3$ derivative.[7,35,44]

Experimental

All chemicals were purchased from Alfa Aesar, Deutero, Fisher Chemicals, TCI, Sigma-Aldrich, and Acros Organics and used without further purification. Solvents were dried according to the literature-known procedures and used freshly distilled.[45] Dry DMF was purchased from Sigma Aldrich. NMR spectra were recorded at room temperature with a Bruker Avance DSX 400 and analysed with the program MestReNova.[46] Magnetic susceptibility measurements were performed on a Quantum Design SQUID magnetometer MPMSXL in a temperature range between 2 and 400 K with an applied field of 1 kOe. All elemental analysis (Elementar vario EL Cube: C, H, and N) were measured at the microanalytical laboratories of the Johannes Gutenberg University Mainz. X-ray diffraction data were collected with STOE STADIVARI at Johannes Gutenberg University Mainz. The structures were solved with ShelXT[47] and refined with ShelXL[48,49] implemented in the program Olex2.[50] The X-ray cif file data are deposited on the Cambridge CCDC database with identification numbers 2348659–2348666.† DFT calculations have been performed using the Gaussian 16 program,[51] using two-hybrid functionals B3LYP and B3LYP*,[44] and the Ahlrichs TZVP basis set[52] for all the atoms present in the complexes.

Ligand synthesis

Synthesis of pyridine-2-carboxylic acid hydrazide. The synthesis procedure was adapted from literature.[24] To a solution of ethyl 2-pyridine carboxylate (13.82 g, 91.43 mmol, 1 eq.) in 125 ml methanol was added hydrazine monohydrate (13.73 g, 274.27 mmol, 3 eq.). The reaction was stirred for 16 hours at room temperature. Afterwards, the mixture was taken to dryness under reduced pressure yielding the desired product as a pale beige white solid in high yields (12.24 g, 89.25 mmol, 98%). **^{1}H NMR** (400 MHz, DMSO, δ (ppm)): 9.86 (s, 1H, N*H*), 8.61–8.60 (m, 1H, pyC*H*), 7.98–7.97 (m, 2H, pyC*H*), 7.58–7.55 (m, 1H, pyC*H*), 4.61 (s, 2H, NH_2).

Synthesis of benzoic acid hydrazide. The synthesis procedure was adapted from literature.[24] To a solution of ethyl benzoate (30.00 g, 0.2 mol, 1.0 eq.) in 200 ml methanol was added hydrazine monohydrate (50.00 ml, 51.50 g, 1.03 mol, 5.1 eq.). The reaction was stirred for 16 hours at 80 °C. Afterwards, the mixture was taken to dryness under reduced pressure and the residual of water was co-evaporated with toluene. The pale-yellow solid was then suspended in 200 ml of diethyl ether and stirred for 30 minutes. The solid was filtered, washed with cold diethyl ether and dried on air to yield the desired product as a pale beige solid (23.65 g, 0.17 mol, 85%). **^{1}H NMR** (400 MHz, DMSO, δ (ppm)): 9.78 (s, 1H, N*H*), 7.83–7.80 (m, 2H, PhC*H*), 7.53–7.42 (m, 3H, PhC*H*), 3.69 (s, 8H, NH_2 + H_2O).

Synthesis of *N*′-(2-chloroacetyl)benzohydrazide. The synthesis procedure was adapted from literature.[24] Benzoic acid hydrazide (23.50 g, 172.57 mmol, 1 eq.) was suspended in 600 ml diethyl ether and cooled to 0 °C. To this solution was added chloroacetyl chloride (23.38 g, 16.47 ml, 207.08 mmol, 1.2 eq.), dissolved in 150 ml diethyl ether, dropwise keeping the temperature below 34 °C. The reaction mixture was stirred for 16 hours at room temperature. The colourless solid was filtered and washed with cold diethyl ether to yield the desired product as colourless solid (35.09 g, 165.80 mmol, 96%). The product was proceeded to the next step without further characterization.

Synthesis of *N*′-(chloroacetyl)-2-pyridinecarboxylic acid hydrazide hydrochloride. The synthesis procedure was adapted from literature.[24] Pyridine-2-carboxylic acid hydrazide (12.24 g, 89.25 mmol, 1 eq.) was suspended in 500 ml diethyl ether and cooled to 0 °C. To this solution was added chloroacetyl chloride (11.08 g, 7.90 ml, 98.18 mmol, 1.1 eq.) dropwise keeping the temperature below 34 °C. The reaction mixture was stirred for 16 hours at room temperature. The colourless solid was filtered and washed with cold diethyl ether to yield the desired product as colourless solid in high yields (21.65 g, 86.5 mmol, 97%). **^{1}H NMR** (400 MHz, DMSO, δ (ppm)): 9.86 (s, 1H, N*H*), 8.61–8.60 (m, 1H, pyC*H*), 7.98–7.97 (m, 2H, pyC*H*), 7.58–7.55 (m, 1H, pyC*H*), 4.61 (s, 2H, NH_2).

Synthesis of 2-(chloromethyl)-5-(pyridine-2-yl)-1,3,4-oxadiazole. The synthesis procedure was adapted from literature.[20,21,24] *N*′-(Chloroacetyl)-2-pyridinecarboxylic acid hydrazide hydrochloride (10.00 g, 39.98 mmol, 1 eq.) was dissolved in 500 ml acetonitrile under an inert atmosphere. To this solution triphenylphosphine (20.97 g, 79.99 mmol, 2 eq.), triethylamine (12.14 g, 16.63 ml, 119.94 mmol, 3 eq.) and carbon tetrachloride (24.61 g, 15.48 ml, 159.95 mmol, 4 eq.) were added simultaneously. The reaction was stirred for 16 hours keeping the inert atmosphere. The solvent was removed completely to yield a black solid as crude product. Column chromatography (SiO_2, chloroform) afforded 23.66 g of a mixture of the desired product 2-(chloromethyl)-5-(pyridine-2-yl)-1,3,4-oxadiazole and triphenylphosphine oxide

(TPPO) as beige solid which was used without any more purification for further reactions. **^{1}H NMR** (400 MHz, $CDCl_3$, δ (ppm)): 8.80 (d, 1H, pyC*H*), 8.27 (d, 1H, pyC*H*), 7.93–7.89 (m, 1H, pyC*H*), 7.93–7.44 (m, 37H, pyC*H* + TPPO), 4.81 (s, 2H, CH_2).

Synthesis of 2-(chloromethyl)-5-phenyl-1,3,4-oxadiazole. The synthesis procedure was adapted from literature.[24] *N*′-(2-Chloroacetyl)benzohydrazide (15.00 g, 70.88 mmol, 1 eq.) was dissolved in 500 ml acetonitrile under an inert atmosphere. To this solution triphenylphosphine (37.18 g, 141.76 mmol, 2 eq.), triethylamine (21.51 g, 29.47 ml, 212.64 mmol, 3 eq.) and carbon tetrachloride (43.61 g, 27.43 ml, 283.52 mmol, 4 eq.) were added simultaneously. The reaction was stirred for 16 hours keeping the inert atmosphere. The solvent was removed completely to yield a black solid as crude product. Column chromatography (SiO_2, chloroform) afforded 30.33 g of a mixture of the desired product and triphenylphosphine oxide (TPPO) as beige solid which was used without any more purification for further reactions. **^{1}H NMR** (400 MHz, $CDCl_3$, δ (ppm)): 8.08 (d, 2H, PhC*H*), 7.69–7.44 (m, 46H, 3PhC*H* + TPPO), 4.78 (s, 2H, CH_2).

Synthesis of Bis[(2-pyridyl)methyl]amine. This product was synthesized as reported in the literature.[24] Pyridine-2-carboxaldehyde (3.21 g, 30.00 mmol, 1.0 eq.) and 2-aminomethylpyridine (3.24 g, 30.00 mmol, 1.0 eq.) were dissolved in 200 ml methanol and stirred at room temperature for 4 hours. After cooling the mixture to 0 °C, sodium borohydride (3.03 g, 80.10 mmol, 2.67 eq.) was added portion wise and the reaction mixture stirred for 16 hours at room temperature. The solvent was removed under reduced pressure. The residue was taken up in 100 ml of water and extracted four times with 60 ml chloroform. The combined organic extracts were dried over magnesium sulphate and taken to dryness to afford the desired product as orange oil in high yields (5.85 g, 29.34 mmol, 98%). **^{1}H NMR** (400 MHz, $CDCl_3$, δ (ppm)): 8.54 (d, 2H, pyC*H*), 7.65–7.61 (m, 2H, pyC*H*), 7.34 (d, 2H, pyC*H*), 7.16–7.13 (m, 2H, pyC*H*), 3.97 (s, 4H, CH_2).

Synthesis of 2-(2-pyridyl)-5-[*N*,*N*-bis(2-pyridylmethyl)aminomethyl]-1,3,4-oxadiazole ($L^{TetraPy-ODA}$). The synthesis procedure was adapted from literature.[24] Bis[(2-pyridyl)methyl]amine (6.03 g, 30.27 mmol, 1.5 eq.) and potassium carbonate (6.98 g, 50.45 mmol, 2.5 eq.) were suspended in 400 ml acetonitrile under an inert atmosphere and heated to 70 °C. To this solution was added 2-(chloromethyl)-5-(pyridin-2-yl)-1,3,4-oxadiazole (3.95 g, 20.18 mmol, 1 eq.), dissolved in 250 ml of acetonitrile. The reaction mixture was stirred vigorously at 70 °C for 16 hours. The solid was filtered and the excess solvent was removed from the filtrate under reduced pressure to afford a brown solid as crude product. Column chromatography (SiO_2, chloroform/methanol (29 : 1)) yielded $L^{TetraPy-ODA}$ as an orange oil which crystallizes after several days (4.87 g, 19.93 mmol, 67%). **^{1}H NMR** (400 MHz, $CDCl_3$, COSY, δ (ppm)): 8.77 (d, 1H, pyC*H*), 8.53 (d, 2H, pyC*H*), 8.22 (d, 1H, pyC*H*), 7.88 (td, 1H, pyC*H*), 7.68–7.63 (m, 2H, pyC*H*), 7.58 (d, 2H, pyC*H*), 7.46 (dd, 1H, pyC*H*), 7.17–7.14 (m, 2H, pyC*H*), 4.19 (s, 2H, ODA-CH_2), 4.04 (s, 4H, Py–CH_2). **^{13}C NMR** (101 MHz, $CDCl_3$, HSQC, HMBC, δ (ppm)): 165.00, 164.28, 158.22, 150.25, 149.20, 143.42, 137.25, 136.64, 125.87, 123.30, 123.13, 122.30, 59.76 (*C*H$_2$), 47.97 (*C*H$_2$). **FT-IR**: $\tilde{\nu}$ (cm^{-1}) = 3055, 3008, 2984, 2946, 2917, 2887, 2838, 1675, 1587, 1567, 1557, 1545, 1515, 1473, 1456, 1431, 1375, 1365, 1360, 1340, 1323, 1308, 1297, 1286, 1247, 1220, 1148, 1100, 1087, 1045, 1022, 1012, 994, 974, 959, 894, 868, 856, 844, 797, 787, 777, 753, 743, 708, 659, 640, 632, 617, 610, 506, 487, 477, 461.

Synthesis of 2-phenyl-5-[*N*,*N*-bis(2-pyridylmethyl)aminomethyl]-1,3,4-oxadiazole ($L^{TetraPh-ODA}$). The synthesis procedure was adapted from literature.[24] Bis[(2-phenyl)methyl] amine (9.12 g, 45.77 mmol, 1.5 eq.) and potassium carbonate (10.56 g, 76.28 mmol, 2.5 eq.) were suspended in 250 ml acetonitrile under an inert atmosphere and heated to 70 °C. To this solution was added **28** (5.97 g, 30.51 mmol, 1 eq.), together with its side product triphenylphosphine oxide (24.36 g, 87.56 mmol) (see Chapter 6.3.26), dissolved in 400 ml of acetonitrile. The reaction mixture was stirred vigorously at 70 °C for 16 hours. The solid was filtered and the excess solvent from the filtrate was removed under reduced pressure to afford a brown solid as crude product. Column chromatography (SiO_2, chloroform/methanol (49 : 1)) yielded $L^{TetraPh-ODA}$ as bright brown oil which crystallizes after several days (7.94 g, 22.21 mmol, 78%). **^{1}H NMR** (400 MHz, $CDCl_3$, δ (ppm)): 8.56–8.54 (m, 2H, pyC*H*), 8.05–8.03 (m, 2H, pyC*H*), 8.69 (dt, 2H, pyC*H*), 7.60–7.48 (m, 5H, PhC*H* + pyC*H*), 7.20–7.16 (m, 2H, pyC*H*), 4.15 (s, 2H, ODA-CH_2), 4.06 (s, 4H, Py–CH_2). **^{13}C NMR** (101 MHz, $CDCl_3$, δ (ppm)): 165.11, 164.02, 158.22, 149.18, 136.62, 131.70, 129.00, 126.89, 123.75, 123.19, 122.30, 59.90 (*C*H$_2$), 47.95 (*C*H$_2$). **FT-IR**: $\tilde{\nu}$ (cm^{-1}) = 3061, 3009, 2948, 2932, 2900, 2853, 1673, 1607, 1589, 1561, 1548, 1490, 1473, 1447, 1433, 1412, 1393, 1367, 1355, 1326, 1311, 1287, 1249, 1206, 1150, 1128, 1085, 1070, 1044, 1007, 994, 984, 975, 958, 942, 919, 896, 877, 831, 771, 755, 744, 706, 685, 652, 641, 631, 612, 514, 488, 471, 445, 403.

Complexes synthesis

$[Fe^{II}_2(L^{TetraPy-ODA})(NCS)]\cdot H_2O$ (C1). The complex synthesis was carried out in inert gas atmosphere. The precursor complex $[Fe(py)_4(NCS)_2]$ (49 mg, 0.1 mmol, 1 eq.) was dissolved in 3 mL acetonitrile and $L^{TetraPy-ODA}$ (36 mg, 0.1 mmol, 1 eq.) was dissolved in 2 ml acetonitrile. The solution was mixed and stirred together for 30 minutes. The solution was filtered using a syringe filter and left undisturbed for slow evaporation. After three days, yellow block shaped orange crystals suitable for X-ray were obtained. The crystals obtained were collected by filtration, washed with diethyl ether and dried in air (13.45 mg, 0.025 mmol, 25%). **FT-IR**: $\tilde{\nu}$ (cm^{-1}) = 3471, 3063, 2062, 2030, 1605, 1546, 1487, 1440, 1292, 1084, 1057, 1025, 977, 879, 778, 761, 737, 708, 646, 522, 478, 424, 411. Elemental analysis calculated for $C_{22}H_{18}FeN_8OS_2\cdot H_2O$: C, 48.18; H, 3.68; N, 20.43; Found, C, 48.37; H, 3.46; N, 20.74.

$[Fe^{II}_2(L^{TetraPy-ODA})(NCSe)]\cdot 0.15\ CH_3CN\cdot 1.5\ H_2O$ (C2). The complex synthesis was carried out in inert gas atmosphere. The precursor complex $[Fe(py)_4(NCSe)_2]$ (58 mg, 0.1 mmol, 1 eq.) was dissolved in 3 ml acetonitrile and $L^{TetraPy-ODA}$ (36 mg,

0.1 mmol, 1 eq.) was dissolved in 2 ml acetonitrile. The solution was mixed and stirred together for 30 minutes. The solution was filtered using a syringe filter and left undisturbed for slow evaporation. After one week, red block-shaped crystals suitable for X-ray were obtained. The crystals obtained were collected by filtration, washed with diethyl ether and dried in air (29.54 mg, 0.047 mmol, 47%). **FT-IR:** $\tilde{\upsilon}$ (cm^{-1}) = 3054, 2904, 2846, 2684, 2307, 2198, 2163, 2059, 1946, 1601, 1569, 1552, 1475, 1457, 1440, 1425, 1410, 1386, 1350, 1332, 1301, 1280, 1247, 1153, 1118, 1097, 1048, 1017, 992, 972, 957, 899, 882, 852, 817, 795, 757, 737, 705, 640, 619, 532, 509, 480, 418. Elemental analysis calculated for $C_{22}H_{18}FeN_8OSe_2 \cdot 0.15\ CH_3CN \cdot 1.5\ H_2O$: C, 41.21; H, 3.31; N, 17.22. Found, C, 41.49; H, 3.54; N, 16.82.

$[Fe^{II}_2(L^{TetraPy-ODA})(NCBH_3)] \cdot 2H_2O$ (C3). The complex synthesis was carried out in an inert gas atmosphere. The precursor complex $[Fe(py)_4(NCBH_3)_2]$ (45 mg, 0.1 mmol, 1 eq.) was dissolved in 3 ml acetonitrile and $L^{TetraPy-ODA}$ (36 mg, 0.1 mmol, 1 eq.) was dissolved in 2 ml acetonitrile. The solution was mixed and stirred together for 30 minutes. The solution was filtered using a syringe filter and left undisturbed for slow evaporation. After one week, green block-shaped crystals suitable for X-ray were obtained. The crystals obtained were collected by filtration, washed with diethyl ether and dried in air (16.98 mg, 0.034 mmol, 34%). **FT-IR:** $\tilde{\upsilon}$ (cm^{-1}) = 3489, 3073, 2060, 1709, 1666, 1603, 1568, 1474, 1445, 1336, 1289, 1258, 1240, 1160, 1093, 1047, 1023, 853, 787, 763, 707, 694, 647, 541, 481, 448, 416. Elemental analysis calculated for $C_{22}H_{24}B_2FeN_8O \cdot 2H_2O$: C, 49.86; H, 5.33; N, 21.14. Found, C, 49.83; H, 5.03; N, 21.40.

$[Fe^{II}_2(L^{TetraPh-ODA})(NCS)] \cdot 1.75H_2O$ (C4). The following reaction was carried out in a glovebox under an inert atmosphere. The precursor complex $[Fe(py)_4(NCS)_2]$ (49 mg, 0.1 mmol, 1 eq.) was dissolved in 3 mL acetonitrile and $L^{TetraPh-ODA}$ (36 mg, 0.1 mmol, 1 eq.) was dissolved in 2 ml acetonitrile. The solution was mixed and stirred together for 30 minutes. The solution was filtered using a syringe filter and left undisturbed for slow evaporation. After three days, orange block-shaped crystals suitable for X-ray were obtained. The crystals obtained were collected by filtration, washed with diethyl ether and dried in air (27.91 mg, 0.053 mmol, 53%). **FT-IR:** $\tilde{\upsilon}$ (cm^{-1}) = 3061, 3008, 2906, 2849, 2059, 1971, 1602, 1590, 1570, 1554, 1479, 1439, 1387, 1368, 1351, 1333, 1314, 1300, 1285, 1247, 1224, 1152, 1121, 1099, 1069, 1047, 1018, 993, 974, 956, 927, 898, 881, 853, 798, 778, 756, 736, 707, 690, 640, 614, 510, 477, 435, 418, 404. Elemental analysis calculated for $C_{23}H_{19}FeN_7OS_2 \cdot 1.75\ H_2O$: C, 49.25; H, 4.04; N, 17.48. Found, C, 49.22; H, 3.62; N, 17.06.

$[Fe^{II}_2(L^{TetraPh-ODA})(NCSe)] \cdot 0.4Et_2O \cdot H_2O$ (C5). The complex synthesis was carried out in inert gas atmosphere. The precursor complex $[Fe(py)_4(NCSe)_2]$ (58 mg, 0.1 mmol, 1 eq.) was dissolved in 3 ml acetonitrile and $L^{TetraPh-ODA}$ (36 mg, 0.1 mmol, 1 eq.) was dissolved in 2 ml acetonitrile. The solution was mixed and stirred together for 30 minutes. The solution was filtered using a syringe filter and left undisturbed for slow evaporation. After one-week, red block shaped crystals suitable for X-ray were obtained. The crystals obtained were collected by filtration, washed with diethyl ether and dried in air (45.63 mg, 0.073 mmol, 73%). **FT-IR:** $\tilde{\upsilon}$ (cm^{-1}) = 2945, 2903, 2847, 2060, 1970, 1944, 1602, 1579, 1572, 1555, 1480, 1450, 1439, 1386, 1350, 1333, 1313, 1300, 1283, 1248, 1224, 1152, 1120, 1113, 1099, 1069, 1047, 1034, 1019, 992, 974, 966, 956, 898, 880, 850, 817, 779, 756, 736, 707, 690, 640, 511, 479, 418. Elemental analysis calculated for $C_{23}H_{19}FeN_7OSe_2 \cdot 0.4C_4H_{10}O \cdot H_2O$: C, 44.04; H, 3.76; N, 14.61. Found, C, 43.62; H, 3.53; N, 14.29.

$[Fe^{II}_2(L^{TetraPh-ODA})(NCBH_3)] \cdot 1.5H_2O$ (C6). The complex synthesis was carried out in an inert gas atmosphere. The precursor complex $[Fe(py)_4(NCBH_3)_2]$ (45 mg, 0.1 mmol, 1 eq.) was dissolved in 3 ml acetonitrile and $L^{TetraPh-ODA}$ (36 mg, 0.1 mmol, 1 eq.) was dissolved in 2 ml acetonitrile. The solution was mixed and stirred together for 30 minutes. The solution was filtered using a syringe filter and left undisturbed for slow evaporation. After one week, green block-shaped crystals suitable for X-ray were obtained. The crystals obtained were collected by filtration, washed with diethyl ether and dried in air (27.38 mg, 0.056 mmol, 56%). **FT-IR:** $\tilde{\upsilon}$ (cm^{-1}) = 3030, 2958, 2919, 2352, 2328, 2177, 1604, 1584, 1574, 1557, 1481, 1440, 1427, 1390, 1355, 1333, 1320, 1304, 1287, 1250, 1223, 1153, 1118, 1112, 1098, 1052, 1044, 1021, 988, 960, 892, 883, 855, 817, 776, 764, 735, 704, 686, 642, 510, 480, 418. Elemental analysis calculated for $C_{23}H_{25}B_2FeN_7O \cdot 1.5H_2O$: C, 53.13; H, 5.43; N, 18.86. Found, C, 52.75; H, 5.08; N, 18.60.

$[Fe^{II}_2(L^{TetraPh})](ClO_4)_4 \cdot CH_3NO_2 \cdot 1.5\ H_2O$ (C7). The reaction was carried out under aerobic conditions. The ligand $L^{TetraPh-ODA}$ (36 mg, 0,1 mmol, 1 eq.) was dissolved in 5 ml of nitromethane. To this solution $Fe(ClO_4)_2 \cdot nH_2O$ (27 mg, 0,1 mmol, 1 eq.) was added as a solid. The reaction solution changed instantaneously to yellow. The reaction mixture was stirred for 30 minutes and filtered. The filtrate was set undisturbed for slow evaporation. Yellow crystalline product suitable for X-ray was obtained after one week in very low yields (5.01 mg, 0.004 mmol, 5%). **FT-IR:** $\tilde{\upsilon}$ (cm^{-1}) = 3079, 2961, 2935, 2005, 1652, 1636, 1609, 1587, 1572, 1555, 1517, 1506, 1487, 1459, 1443, 1430, 1375, 1362, 1319, 1312, 1292, 1253, 1224, 1163, 1151, 1072, 1021, 1003, 962, 948, 930, 897, 886, 878, 835, 799, 761, 748, 716, 706, 665, 648, 620, 511, 485, 458, 419, 409. Elemental analysis calculated for $C_{40}H_{36}Cl_4Fe_2N_{12}O_{18} \cdot CH_3NO_2 \cdot 1.5H_2O$: C, 37.47; H, 3.22; N, 13.85. Found, C, 37.19; H, 3.32; N, 13.99.

Conflicts of interest

There are no conflicts to declare.

Acknowledgements

S. U. S., J. E., L. W., L. M. C. and E. R. sincerely thank JGU Mainz for the funding and support. E. G. thanks the CSIR-UGC for providing a PhD fellowship. K. R. V. thanks the IISER Mohali-High Performing Computing Facility for providing

computing resources and also thanks SERB for providing start-up research grant funding (SRG/2023/000286).

References

1 M. Sánchez, L. Sabio, N. Gálvez, M. Capdevila and J. M. Dominguez-Vera, *IUBMB Life*, 2017, **69**, 382–388.
2 P. A. Frey and G. H. Reed, *ACS Chem. Biol.*, 2012, **7**(9), 1477–1481.
3 J. Hohenberger, K. Ray and K. Meyer, *Nat. Commun.*, 2012, **3**(1), 720.
4 M. Keilwerth, W. Mao, M. Malischewski, S. A. V. Jannuzzi, K. Breitwieser, F. W. Heinemann, A. Scheurer, S. Debeer, D. Munz, E. Bill and K. Meyer, *Nat. Chem.*, 2024, 1–7.
5 L. Cambi and L. Szegö, *Ber. Dtsch. Chem. Ges. B*, 1931, **64**, 2591–2598.
6 M. A. Halcrow, *Spin-Crossover Materials: Properties and Applications*, John Wiley and Sons, 2013.
7 P. Gütlich, Y. Garcia and H. A. Goodwin, *Chem. Soc. Rev.*, 2000, **29**, 419–427.
8 H. L. C. Feltham, A. S. Barltrop and S. Brooker, *Coord. Chem. Rev.*, 2017, **344**, 26–53.
9 S. Brooker, *Chem. Soc. Rev.*, 2015, **44**, 2880–2892.
10 D. J. Harding, P. Harding and W. Phonsri, *Coord. Chem. Rev.*, 2016, **313**, 38–61.
11 S. Sundaresan, I. A. Kühne, C. Evesson, M. M. Harris, A. J. Fitzpatrick, A. Ahmed, H. Müller-Bunz and G. G. Morgan, *Polyhedron*, 2021, **208**, 115386.
12 J. Olguín, *Coord. Chem. Rev.*, 2020, **407**, 213148.
13 I. Krivokapic, M. Zerara, M. L. Daku, A. Vargas, C. Enachescu, C. Ambrus, P. Tregenna-Piggott, N. Amstutz, E. Krausz and A. Hauser, *Coord. Chem. Rev.*, 2007, **251**, 364–378.
14 S. Hayami, Y. Komatsu, T. Shimizu, H. Kamihata and Y. H. Lee, *Coord. Chem. Rev.*, 2011, **255**, 1981–1990.
15 N. A. A. M. Amin, S. M. Said, M. F. M. Salleh, A. M. Afifi, N. M. J. N. Ibrahim, M. M. I. M. Hasnan, M. Tahir and N. Z. I. Hashim, *Inorg. Chim. Acta*, 2023, **544**, 121168.
16 A. B. Gaspar, V. Ksenofontov, M. Seredyuk and P. Gütlich, *Coord. Chem. Rev.*, 2005, **249**, 2661–2676.
17 A. B. Gaspar and M. Seredyuk, *Coord. Chem. Rev.*, 2014, **268**, 41–58.
18 A. Enriquez-Cabrera, A. Rapakousiou, M. Piedrahita Bello, G. Molnár, L. Salmon and A. Bousseksou, *Coord. Chem. Rev.*, 2020, **419**, 213396.
19 K. Senthil Kumar and M. Ruben, *Coord. Chem. Rev.*, 2017, **346**, 176–205.
20 C. Köhler and E. Rentschler, *Eur. J Inorg. Chem.*, 2016, 1955–1960.
21 S. Sundaresan, J. Eppelsheimer, L. M. Carrella and E. Rentschler, *Crystals*, 2022, **12**, 404.
22 J. Klingele, D. Kaase, M. Schmucker, Y. Lan, G. Chastanet and J. F. Letard, *Inorg. Chem.*, 2013, **52**, 6010.
23 P. Zoufalý, A. Kliuikov, E. Čižmár, I. Císařová and R. Herchel, *Eur. J. Inorg. Chem.*, 2021, 1190–1199.
24 S. Sundaresan, J.-G. Becker, J. Eppelsheimer, A. E. Sedykh, L. Carrella, K. Müller-Buschbaum and E. Rentschler, *Dalton Trans.*, 2023, **52**, 13181–13189.
25 S. Sundaresan, J. Kiehl, L. M. Carrella and E. Rentschler, *Cryst. Growth Des.*, 2023, **23**(3), 1648–1655.
26 B. Fei, X. Q. Chen, Y. De Cai, J. K. Fang, M. L. Tong, J. Tucek and X. Bao, *Inorg. Chem. Front.*, 2018, **5**, 1671–1676.
27 C. F. Herold, L. M. Carrella and E. Rentschler, *Eur. J. Inorg. Chem.*, 2015, 3632–3636.
28 C. F. Herold, S. I. Shylin and E. Rentschler, *Inorg. Chem.*, 2016, **55**, 6414–6419.
29 H. S. Scott, R. W. Staniland and P. E. Kruger, *Coord. Chem. Rev.*, 2018, **362**, 24–43.
30 U. Habarakada, T. Boonprab, P. Harding, K. S. Murray, W. Phonsri, S. M. Neville, M. Ahmed and D. J. Harding, *Cryst. Growth Des.*, 2022, **22**, 4895–4905.
31 R. W. Hogue, R. G. Miller, N. G. White, H. L. C. Feltham, G. N. L. Jameson and S. Brooker, *Chem. Commun.*, 2014, **50**, 1435–1437.
32 S. Sundaresan and S. Brooker, *Inorg. Chem.*, 2023, **62**(31), 12192–12202.
33 S. Alvarez, *Chem. – Eur. J.*, 2020, **26**, 4350–4377.
34 J. Cirera and F. Paesani, *Inorg. Chem.*, 2012, **51**(15), 8194–8201.
35 J. Cirera, M. Via-Nadal and E. Ruiz, *Inorg. Chem.*, 2018, **57**(22), 14097–14105.
36 S. De, L.-M. Chamoreau, H. El Said, Y. Li, A. Flambard, M.-L. Boillot, S. Tewary, G. Rajaraman, J. Manuel Seco and R. Lescouëzec, *Front. Chem.*, 2018, **1**, 326.
37 M. Schmidt, D. Wiedemann, B. Moubaraki, N. F. Chilton, K. S. Murray, K. R. Vignesh, G. Rajaraman and A. Grohmann, *Eur. J. Inorg. Chem.*, 2013, 958–967.
38 S. Ye and F. Neese, *Inorg. Chem.*, 2010, **49**, 772–774.
39 D. Vidal, J. Cirera and J. Ribas-Arino, *Phys. Chem. Chem. Phys.*, 1249, **25**, 12490.
40 K. P. Kepp, *Coord. Chem. Rev.*, 2013, **257**, 196–209.
41 E. Jakubikova and D. N. Bowman, *Acc. Chem. Res.*, 2015, **48**(5), 1441–1449.
42 W. Honsri, D. S. Macedo, K. R. Vignesh, G. Rajaraman, C. D. Avies, G. N. L. Jameson, B. Moubaraki, J. S. Ward, P. E. Kruger, G. Chastanet and K. S. Murray, *Chem. – Eur. J.*, 2017, **23**, 7052–7065.
43 J. M. Holland, J. A. Mcallister, Z. Lu, C. A. Kilner, M. Thornton-Pett and M. A. Halcrow, *Chem. Commun.*, 2001, 577–578.
44 K. P. Kepp, *Inorg. Chem.*, 2016, **55**, 17.
45 W. L. F. Armarego, *Purification of laboratory chemicals*, 2017, pp. 95–634.
46 J. C. Cobas and F. J. Sardina, *Concepts Magn. Reson., Part A*, 2003, 80–96.
47 G. M. Sheldrick, *Acta Crystallogr.*, 2015, **71**, 3–8.
48 G. M. Sheldrick and T. R. Schneider, *Methods Enzymol.*, 1997, **277**, 319–343.
49 G. M. Sheldrick, *Acta Crystallogr., Sect. C: Struct. Chem.*, 2015, **71**, 3–8.

50 O. V. Dolomanov, L. J. Bourhis, R. J. Gildea, J. A. K. Howard and H. Puschmann, *J. Appl. Crystallogr.*, 2009, **42**, 339–341.
51 M. J. Frisch, G. W. Trucks, H. B. Schlegel, G. E. Scuseria, M. A. Robb, J. R. Cheeseman, G. Scalmani, V. Barone, G. A. Petersson, H. Nakatsuji, X. Li, M. Caricato, A. V. Marenich, J. Bloino, B. G. Janesko, R. Gomperts, B. Mennucci, H. P. Hratchian, J. V. Ortiz, A. F. Izmaylov, J. L. Sonnenberg, D. Williams-Young, F. Ding, F. Lipparini, F. Egidi, J. Goings, B. Peng, A. Petrone, T. Henderson, D. Ranasinghe, V. G. Zakrzewski, J. Gao, N. Rega, G. Zheng, W. Liang, M. Hada, M. Ehara, K. Toyota, R. Fukuda, J. Hasegawa, M. Ishida, T. Nakajima, Y. Honda, O. Kitao, H. Nakai, T. Vreven, K. Throssell, J. A. Montgomery Jr., J. E. Peralta, F. Ogliaro, M. J. Bearpark, J. J. Heyd, E. N. Brothers, K. N. Kudin, V. N. Staroverov, T. A. Keith, R. Kobayashi, J. Normand, K. Raghavachari, A. P. Rendell, J. C. Burant, S. S. Iyengar, J. Tomasi, M. Cossi, J. M. Millam, M. Klene, C. Adamo, R. Cammi, J. W. Ochterski, R. L. Martin, K. Morokuma, O. Farkas, J. B. Foresman and D. J. Fox, *Gaussian 16, rev. B.01*, Gaussian, Inc., Wallingford, CT, 2016.
52 F. Weigend and R. Ahlrichs, *Phys. Chem. Chem. Phys.*, 2005, **7**, 3297–3305.